Available online at www.sciencedirect.com
ScienceDirect
Journal of Sound and Vibration 320 (2009) 893–914
JOURNAL OF SOUND AND VIBRATION
www.elsevier.com/locate/jsvi

Dynamic train–turnout interaction in an extended frequency range using a detailed model of track dynamics

Elias Kassa* , Jens C.O. Nielsen

CHARMEC/Department of Applied Mechanics, Chalmers University of Technology, SE-412 96 Gothenburg, Sweden

Received 6 January 2008; received in revised form 27 August 2008; accepted 28 August 2008
Handling Editor: C.L. Morfey
Available online 8 October 2008

Abstract

A time domain solution method for general three-dimensional dynamic interaction of train and turnout (switch and crossing) that accounts for excitation in an extended frequency range (up to several hundred Hz) is proposed. Based on a finite element (FE) model of a standard turnout design, a complex-valued modal superposition of track dynamics is applied using the first 500 eigenmodes of the turnout model. The three-dimensional model includes the distribution of structural flexibility along the turnout, such as bending and torsion of rails and sleepers, and the variations in rail cross-section and sleeper length. Convergence of simulation results is studied while using an increasing number of eigenmodes. It is shown that modes with eigenfrequencies up to at least 200 Hz have a significant influence on the magnitudes of the wheel–rail contact forces. Results from using a simplified track model with a commercial computer program for low-frequency vehicle dynamics are compared with the results from using the detailed FE model in conjunction with the proposed method.

1. Introduction

Turnouts (switches and crossings) are essential components of railway infrastructure because they provide flexibility to traffic operation. They are comprised a switch panel and a crossing panel, which are connected by a closure panel, see Fig. 1. However, according to maintenance databases, turnouts stand for a large contribution of reported track faults and this requires high maintenance costs [1].

Dynamic train–track interaction in turnouts is far more complex than on ordinary tangent or curved tracks. Large wheelset displacements and multiple wheel–rail contacts are common. Severe impact loads with significant contributions from high-frequency dynamic interaction are generated, when nominal wheel–rail contact conditions are disturbed at various locations in the turnout. The largest disturbances occur when the wheels are transferred from stock rail to switch rail in the switch panel and in the crossing panel when the wheels pass the gap between wing rail and nose rail. Due to wear and plastic deformation, surface irregularities with wavelengths of 1–10 cm may be present on the running surfaces of wheels and rails. This calls for models

*Corresponding author. Present address: Rail Technology Unit, Manchester Metropolitan University, Department of Engineering & Technology, John Dalton Building, Chester Street, Manchester M1 5GD, UK. Tel.: +44 161 247 6019; fax: +44 161 247 1633.
E-mail addresses: e.kassa@mmu.ac.uk (E. Kassa), jens.nielsen@chalmers.se (J.C.O. Nielsen).

0022-460X/$ - see front matter © 2008 Elsevier Ltd. All rights reserved.
doi:10.1016/j.jsv.2008.08.028

Nomenclature

In the current paper, one dot (˙) above a vector denotes the first time derivative of the vector and two dots (¨) denote the second time derivative. Complex quantities are indicated by an underbar. Quantities in local beam coordinate systems are indicated by an overbar. A tilde (˜) above a vector denotes the skew-symmetric matrix associated with the vector that means a cross product $\mathbf{r} \times \mathbf{F}$ can be written as $\tilde{\mathbf{r}}\mathbf{F}$ by using the skew-symmetric matrix. Subscripts v, r and w denote vehicle, rail and wheel models, respectively. Matrices and vectors are bold-faced. The abbreviation 'cs' is used for, coordinate system, throughout the paper.

$\underline{a}_n$ modal Foss damping of eigenmode n

$\mathbf{A}_{b-t}$ transformation matrix from local beam coordinate system (cs) to track reference cs

$\mathbf{A}_c$ transformation matrix from track reference cs to contact cs

$\mathbf{A}_{g-t}$ transformation matrix from global cs to track reference cs

$\mathbf{A}_{w-t}$ transformation matrix from local wheel fixed cs to track reference cs

$\underline{\mathbf{A}}$ matrix in state-space formulation

$\underline{b}_n$ modal Foss stiffness of eigenmode n

$\underline{\mathbf{B}}$ matrix in state-space formulation

C_H Hertzian stiffness constant

$\mathbf{C}$ damping matrix

F_n, $F_{n,\text{back}}$ normal contact force between wheel tread and rail and between back of wheel flange and check rail

$\mathbf{F}$ generalized load vector

$\mathbf{F}_c$, $\mathbf{F}_{\text{wr},t}$ contact forces in contact and track reference cs

$\mathbf{F}_i$ nodal forces at node i

$\mathbf{F}_r$ contact forces on rail beam centre line

$\mathbf{F}_w$, $\mathbf{F}_{w,\text{back}}$, $\mathbf{F}_{w,\text{tot}}$ equivalent loading on wheel centre from wheel–rail contact forces, from contact forces on back of wheel flange and from sum of equivalent contact loads in all wheel–rail contacts

$\mathbf{K}$ stiffness matrix

$\mathbf{L}_w$ position vector of wheel contact point in local wheel fixed cs

m_n modal mass of mode n

M number of modes

$\mathbf{M}$ mass matrix

$\mathbf{M}_c$, $\mathbf{M}_{\text{wr},t}$ spin moments in contact and track reference cs

$\mathbf{M}_i$ nodal moments at node i

$\mathbf{M}_r$ spin moments on rail beam centre line

N number of dofs

N_r number of rail dofs

$\mathbf{N}_b$ beam element shape function matrix

$\mathbf{N}_{\text{tot}}$ total mapping matrix for one wheel–rail contact point

p_b point located on the beam axis with finite element rail nodes

p_c wheel–rail contact point

p_r origin of rail fixed cs located on the rail centre line which is 0.75 m from the track centre line

$\mathbf{P}_r$ transformation matrix

$\underline{\mathbf{P}}$ matrix of eigenmodes

$\mathbf{pos}_{\text{rc}}$ global position of contact point on rail surface

$\mathbf{pos}_{\text{wc}}$ global position of contact point on wheel surface

$\underline{\mathbf{q}}$ modal displacement vector

$\mathbf{q}_{v,f}$ generalized flexible body coordinates of the vehicle system

$\underline{\mathbf{Q}}$ modal load vector

$\mathbf{Q}_{v,e}$, $\mathbf{Q}_{v,v}$ externally applied loads and loads due to gyroscopic and circulatory effect of the vehicle system

$\mathbf{r}_c$ position vector of rail contact point with respect to rail centre line

$\mathbf{r}_w$ position vector of wheel contact point with respect to wheel centre in track reference cs

$\bar{\mathbf{r}}_c$ position vector of rail contact point with respect to beam centre line

$\tilde{\mathbf{r}}_{w,\text{back}}$ skew-symmetric matrix associated with vector $\mathbf{r}_{w,\text{back}}$

$\bar{\tilde{\mathbf{r}}}_c$ skew-symmetric matrix associated with vector $\bar{\mathbf{r}}_c$

$\mathbf{R}_r$ global position of rail centre line (origin of rail fixed cs)

$\mathbf{R}_w$ global position of wheel centre (origin of wheel fixed cs)

$\mathbf{S}$ transformation matrix

t time

$\mathbf{T}$ rotational transformation matrix

$\mathbf{u}$ generalized displacement vector

$\mathbf{u}_c$, $\mathbf{u}_{c,\text{back}}$	displacement vector at contact point p_c on rail surface and on check rail surface
$\bar{\mathbf{u}}$	displacement vector in local (body-fixed) cs
$\bar{\mathbf{u}}_b$	displacement vector in point p_b along beam centre line
$\mathbf{x}$	generalized nodal displacement vector
$y_{r,\text{back}}$	position of contact point on check rail with respect to track centre
$y_{w,\text{back}}$	position of contact point on back of wheel flange in track following cs with respect to track centre
$\mathbf{z}$	state-space vector
γ_c	contact angle
$\mathbf{\Delta}_c$, $\mathbf{\Delta}_g$	local deformation vector of wheel and rail surfaces in local contact cs and in global cs
Δt_k	time step at time t_k
δ_n, $\delta_{n,\text{back}}$	normal deformation between wheel face and rail and between back of wheel flange and check rail
ζ_n	relative modal damping of eigenmode n
θ_j	angle of beam element j with respect to global cs
μ, μ_{back}	friction coefficient in wheel–rail interface and in wheel–check rail interface
$\boldsymbol{\rho}^{(n)}$	real-valued eigenvector of eigenmode n
$\underline{\boldsymbol{\rho}}^{(n)}$	complex-valued eigenmode vector of eigenmode n
φ	wheel yaw angle
$\underline{\omega}_n$	complex-valued angular eigenfrequency of eigenmode n
ω_{0n}	real-valued angular eigenfrequency of eigenmode n

of train and turnout that are valid in a wide frequency range up to about 1 kHz. In addition, the assembled model needs to account for vehicle dynamics at low frequencies due to nominal turnout geometry and track irregularities with wavelengths in the order of 1 m.

The necessary detail in modelling of vehicle and track depends on the frequency range of interest. Dynamics of vehicle and track are dominated by motion in different frequency ranges [2]. For example, the first modes of vibration of the bogie frame and the car body occur below 10 Hz, whereas the dynamic stiffness of the track may be relatively constant for frequencies below around 20 Hz. The first mode of vertical vibration of the assembled track superstructure on ballast/subground normally occurs above 50 Hz. Various mathematical models for tangent track dynamics have been reviewed by Grassie [3]. For vertical excitation with frequencies up to about 400 Hz, the rail is represented satisfactorily by an Euler–Bernoulli beam, while for frequencies in the interval 400–4000 Hz the rail is better represented by a Rayleigh–Timoshenko beam. Significant features of the lateral dynamics of a tangent track are resonances involving motion of rails and sleepers laterally on the ballast at about 80 Hz, lateral vibration of the rail on the railpad at about 150 Hz, torsional vibration of the rail on the railpad at about 350 Hz, and the pinned–pinned mode at about 350 Hz.

Traditionally, simulation of a train passing a turnout has been devoted to vehicle ride dynamics in the low-frequency range 0–20 Hz [4–6]. To model track dynamics in this frequency range, one co-following

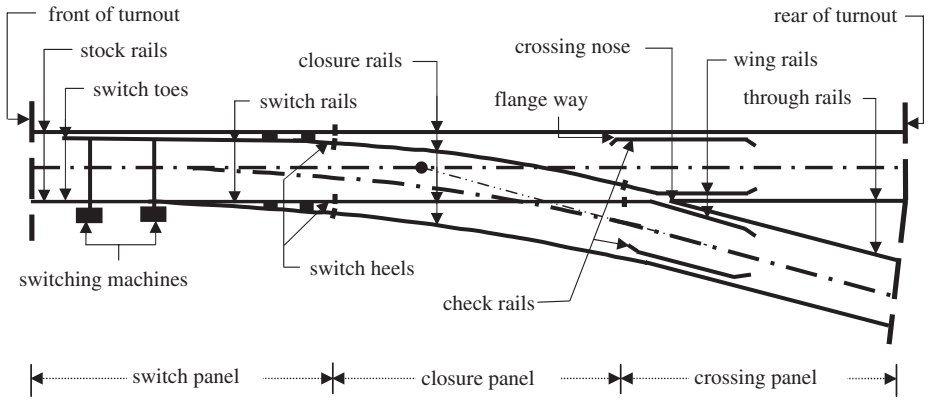

Fig. 1. Components of a turnout.

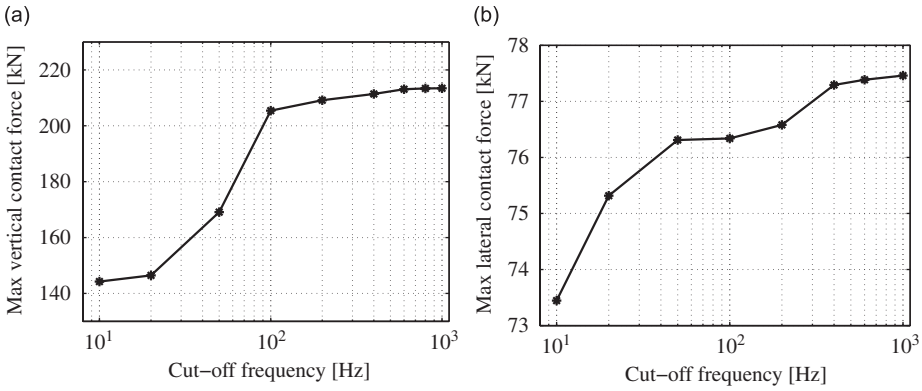

Fig. 2. Maximum measured vertical wheel–rail contact forces in the crossing panel (a) and maximum measured lateral wheel–rail contact forces in the switch panel (b) after low-pass filtering with different cut-off frequencies.

mass-spring-damper model with few degrees-of-freedom (dofs) that is coupled to each wheelset may be sufficient. Several commercial software that include such track models are available for simulation of low-frequency vehicle dynamics [7]. These models are adequate for studies of vehicle motion but they are not useful for understanding dynamics and degradation of track components. For example, bending and torsion of rails and sleepers are not accounted for, and the interaction between adjacent wheelsets that is transmitted through the track is neglected. An accurate prediction of high-frequency impact loads also requires that the structural dynamic flexibility of wheelset and track in a wide frequency range is treated in the model [2].

To quantify the high-frequency content in the wheel–rail contact forces in the switch and crossing panels, contact forces have been measured using an instrumented wheelset [8] and low-pass filtered with different cut-off frequencies. Fig. 2 shows that the high-frequency contribution to the maximum vertical contact force on the crossing is considerable, whereas the high-frequency contribution to the maximum lateral contact force in the switch panel is not as significant. Andersson and Dahlberg [9] calculated vertical impact loads in the crossing. Their study included a finite element (FE) model of the crossing panel and a modal superposition of track dynamics considering frequencies up to 1500 Hz, but their model was restricted to vertical train–track interaction in the main route of the turnout.

In the present study, the model approach in Ref. [9] is extended. A detailed three-dimensional FE model of a railway turnout is built in a commercial software I-DEAS [10]. The undamped model accounts for the structural flexibility of the various rails and sleepers in the turnout. The continuous variations in shape of the rail cross-sections, in length of the sleepers and in sleeper spacing along the turnout are accounted for. These variations have significant influences on the spatial distribution of track stiffness and track inertia. Real-valued eigenfrequencies and eigenmodes of the turnout are calculated and modal damping is added. The modal model of the turnout is implemented in the in-house software DIFF3D [11] for simulation of general (three-dimensional) train–track interaction involving both vertical and lateral track dynamics. The addition of this track model enhances the model for general dynamic interaction between train and turnout that was introduced in Ref. [12].

2. Turnout model

To account for the structural flexibility of the turnout, a FE model of the standard design UIC60-760-1:15 has been built. It is a three-dimensional model that considers displacements (translations and rotations), and forces (and moments) in all three directions.

The model contains structural elements for the rails, railpads, sleepers, and ballast/subgrade, see Fig. 3. The rails and sleepers are modelled by Rayleigh–Timoshenko–Saint-Venant beam elements with three translational and three rotational dofs in each node. The rail in each sleeper bay is divided into eight beam elements. The beam cross-sectional properties change step wise (from one element to the next) to account for the continuous variation in rail cross-section. The variations in length of the sleepers and sleeper spacing are

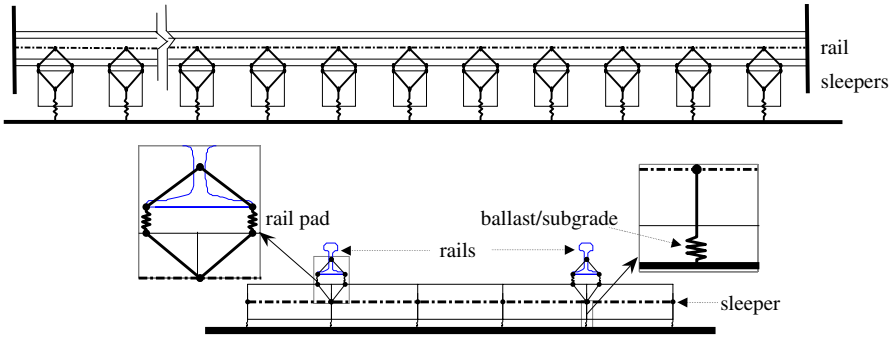

Fig. 3. Principal sketch of FE model of the turnout. Side view (top) and front view (bottom). Each spring element accounts for stiffnesses in three directions.

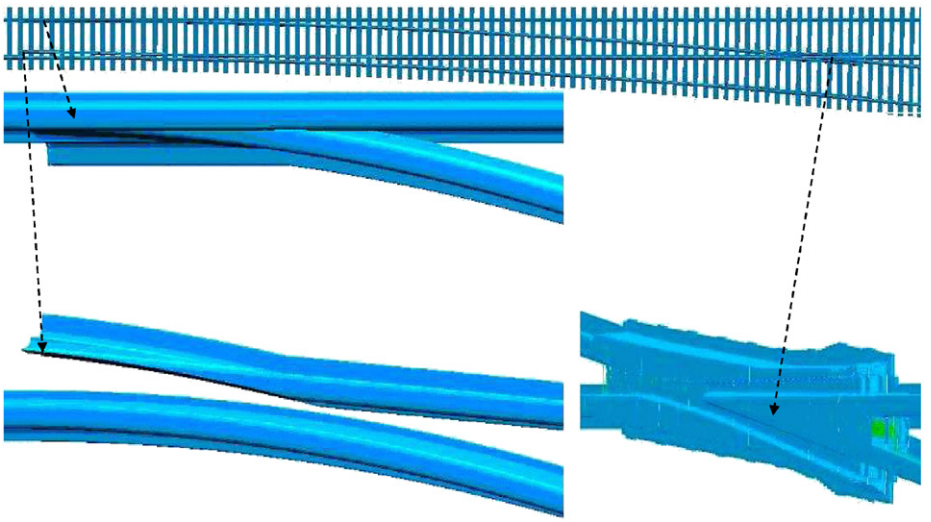

Fig. 4. FE model of the turnout. The model accounts for the variations in rail cross-section and sleeper length along the turnout.

also treated. The FE model of the turnout is shown in Fig. 4. The structural flexibility of the check rails are included using beam elements with six dofs in each node. The check rail beam elements are connected to the sleepers by rigid connections.

To represent each railpad, four linear spring elements are used between adjacent rail and sleeper nodes, see Fig. 3. The four spring elements are positioned at the corners of the railpad to account for both the translational and rotational flexibility of the railpad. To represent the flexibility of the ballast/subgrade, linear spring elements are used under each sleeper, see Fig. 3.

Before the front of the turnout, a tangent track section including 10 sleeper bays is included to reduce the influence of the boundary of the model when the wheel–rail contacts reaches the switch panel. The rails are clamped in all directions at all boundaries of the model. The model contains a total of 99 sleepers with constant cross-sections but with different lengths. The complete FE model consists of beam elements, spring elements and rigid links with a total of $N = 26\,760$ dofs.

2.1. Modal parameters extraction

The modal superposition technique can often be an efficient approach in dynamic analysis of linear and time-invariant structures. The method is used to transform a coupled system of equations of motion into an uncoupled system of equations, see for example Ref. [13]. For a turnout model with N dofs, the N governing

coupled equations of motion with mass $\mathbf{M}$, damping $\mathbf{C}$ and stiffness $\mathbf{K}$ matrices can be expressed as

$$\mathbf{M}\ddot{\mathbf{x}} + \mathbf{C}\dot{\mathbf{x}} + \mathbf{K}\mathbf{x} = \mathbf{F}, \tag{1}$$

where $\mathbf{x}$ is the generalized displacement vector and $\mathbf{F}$ is the generalized load vector. A partition of $\mathbf{x}$ contains the generalized dofs $\mathbf{u}$ belonging to the different rails in the turnout model. Thus, $\mathbf{u} = \mathbf{P}_r\mathbf{x}$, where $\mathbf{P}_r$ is a transformation matrix. The total number of dofs belonging to the rail beam elements is $N_r = 17\,814$.

In cases when the damping of the structure can be assumed to be spatially distributed as a linear combination of the mass and stiffness matrices of the model, the damping is referred to as proportional (Rayleigh) damping. The equations of motion can then be decoupled by use of real-valued eigenmodes. In the general case with non-proportional damping, a state-space formulation of the equations of motion and complex-valued eigenmodes are required. Through modal expansion using $2M$ complex-conjugated eigenmodes ($M \ll N$), the state-space vector $\mathbf{z} = \{\mathbf{u}\ \dot{\mathbf{u}}\}^{\mathrm{T}}$ may be expressed as

$$\mathbf{z} = \underline{\mathbf{P}}\,\underline{\mathbf{q}}, \tag{2}$$

where $\underline{\mathbf{P}}$ is a matrix of eigenmodes $\underline{\boldsymbol{\rho}}^{(n)}$ collected as column vectors

$$\underline{\mathbf{P}} = \begin{bmatrix} \underline{\boldsymbol{\rho}}^{(1)} & \cdots & \underline{\boldsymbol{\rho}}^{(2M)} \\ \mathrm{i}\underline{\omega}_1\underline{\boldsymbol{\rho}}^{(1)} & \cdots & \mathrm{i}\underline{\omega}_{2M}\underline{\boldsymbol{\rho}}^{(2M)} \end{bmatrix}, \tag{3}$$

and $\underline{\omega}_n$ are the complex-valued angular eigenfrequencies. The N coupled second-order equations of motion, Eq. (1), are decoupled into $2M$ first-order equations [13] as

$$\mathrm{diag}(\underline{a}_n)\dot{\underline{\mathbf{q}}} + \mathrm{diag}(\underline{b}_n)\,\underline{\mathbf{q}} = \underline{\mathbf{Q}}, \quad n = 1, 2, \ldots, 2M \ \ (M \ll N), \tag{4}$$

where $\underline{a}_n$ and $\underline{b}_n$ are so-called modal Foss dampings and stiffnesses [13]. In Eq. (4), $\underline{\mathbf{q}}$ and $\underline{\mathbf{Q}}$ represent the modal displacement and modal load vectors for the truncated number of M modes. For a non-singular diagonal matrix $\underline{a}_n$, Eq. (4) can be reformulated as

$$\dot{\underline{\mathbf{q}}} = \underline{\mathbf{A}}\,\underline{\mathbf{q}} + \underline{\mathbf{B}}\,\mathbf{F} \tag{5}$$

with matrices $\underline{\mathbf{A}}$ and $\underline{\mathbf{B}}$ defined as

$$\underline{\mathbf{A}} = -\mathrm{diag}[\underline{b}_n/\underline{a}_n] = \mathrm{diag}[\mathrm{i}\underline{\omega}_n], \quad \underline{\mathbf{B}} = \left[\frac{1}{\underline{a}_n}\underline{\boldsymbol{\rho}}^{(n)\mathrm{T}}\right]. \tag{6}$$

Here, an undamped ($\mathbf{C} = 0$) FE model of the turnout was built using a commercial software [10]. Real-valued eigenfrequencies ω_{0n}, eigenvectors $\boldsymbol{\rho}^{(n)}$ and corresponding modal masses m_n were calculated. To account for the damping in the structure, relative modal damping ζ_n was inserted into the model. Since measurement data of damping in the turnout structure were not available, relative modal damping values according to Ref. [9] were adopted. Relatively large relative damping values $\zeta_n = 0.5$ were used for modes with eigenfrequencies below 400 Hz, while relative damping values $\zeta_n = 0.1$, 0.2 and 0.01 were used for modes with eigenfrequencies in the frequency intervals 400–700, 700–850 and 850–1100 Hz, respectively. The modal Foss dampings $\underline{a}_n$ and stiffnesses $\underline{b}_n$ can then be expressed as, see Ref. [9],

$$\underline{a}_n = \pm\mathrm{i}2m_n\omega_{0n}\sqrt{1-\zeta_n^2},$$

$$\underline{b}_n = 2m_n\omega_{0n}^2\left[(1-\zeta_n^2) \pm \mathrm{i}\zeta_n\sqrt{1-\zeta_n^2}\right]. \tag{7}$$

The complex-valued modal Foss dampings $\underline{a}_n$ and stiffnesses $\underline{b}_n$, together with the real-valued eigenvectors $\boldsymbol{\rho}^{(n)}$ from the FEM software, are used to describe the turnout as a modal component in the in-house computer program DIFF3D [11] that is used to solve the train–turnout interaction problem.

2.2. Transient modal solution using a second-order hold (SOH) method

The transient solution at time t for the initial-value problem in modal coordinates

$$\dot{\underline{\mathbf{q}}} = \underline{\mathbf{A}}\,\underline{\mathbf{q}} + \underline{\mathbf{B}}\,\mathbf{F}, \quad \underline{\mathbf{q}}(t_0) = \underline{\mathbf{q}}_0, \tag{8}$$

can be given in convolution integral form, see Meirovitch [14], as

$$\underline{\mathbf{q}}(t) = \mathrm{e}^{\underline{\mathbf{A}}(t-t_0)}\,\underline{\mathbf{q}}(\mathrm{t}_0) + \int_{t_0}^{t} \mathrm{e}^{\underline{\mathbf{A}}(t-\tau)}\,\underline{\mathbf{B}}\,\mathbf{F}(\tau)\,\mathrm{d}\tau, \tag{9}$$

where $\underline{\mathbf{q}}(t_0)$ is the modal displacement vector at $t = t_0$ and $\mathrm{e}^{\underline{\mathbf{A}}(t-t_0)}$ is the transition matrix.

For the current type of problem, a solution method is developed and discussed by Andersson [11]. A first-order hold (FOH) method was shown to be the most efficient method when compared with the zero-order hold and the midpoint rule methods [11]. Here, the efficiency of a second-order hold (SOH) method is studied.

Expressing Eq. (9) in time-discrete form yields the exact solution in convolution integral form

$$\underline{\mathbf{q}}(t_{k+1}) = \mathrm{e}^{\underline{\mathbf{A}}\,\Delta t_k}\,\underline{\mathbf{q}}(\mathrm{t}_k) + \int_{t_k}^{t_k+\Delta t_k} \mathrm{e}^{\underline{\mathbf{A}}(t_k+\Delta t_k-\tau)}\,\underline{\mathbf{B}}\,\mathbf{F}(\tau)\,\mathrm{d}\tau, \tag{10}$$

where $\Delta t_k = t_{k+1} - t_k$. Using the transformation $\sigma = t_k + \Delta t_k - \tau$, Eq. (10) can be rewritten as

$$\underline{\mathbf{q}}_{k+1} = \mathrm{e}^{\underline{\mathbf{A}}\,\Delta t_k}\underline{\mathbf{q}}_k + \int_0^{\Delta t_k} \mathrm{e}^{\underline{\mathbf{A}}\,\sigma}\,\underline{\mathbf{B}}\,\mathbf{F}(\mathrm{t}_k + \Delta \mathrm{t}_k - \sigma)\,\mathrm{d}\sigma. \tag{11}$$

Truncating the Taylor expansion after the second term leads to a second-order polynomial approximation of the load vector $\mathbf{F}$

$$\mathbf{F}(t_k + \Delta t_k - \sigma) \approx \mathbf{F}_k + \frac{\mathrm{d}\mathbf{F}_k}{\mathrm{d}t}(\Delta t_k - \sigma) + \frac{1}{2}\frac{\mathrm{d}^2\mathbf{F}_k}{\mathrm{d}t^2}(\Delta t_k - \sigma)^2. \tag{12}$$

Using the SOH method, Eq. (11) can be expressed as

$$\underline{\mathbf{q}}_{k+1} = \hat{\underline{\mathbf{A}}}_k\underline{\mathbf{q}}_k + \hat{\underline{\mathbf{B}}}_{k,0}\mathbf{F}_k + \hat{\underline{\mathbf{B}}}_{k,1}\frac{\mathrm{d}\mathbf{F}_k}{\mathrm{d}t} + \hat{\underline{\mathbf{B}}}_{k,2}\frac{\mathrm{d}^2\mathbf{F}_k}{\mathrm{d}t^2}, \tag{13}$$

where

$$\hat{\underline{\mathbf{A}}}_k = \mathrm{e}^{\underline{\mathbf{A}}\,\Delta t_k},$$

$$\hat{\underline{\mathbf{B}}}_{k,0} = \underline{\mathbf{A}}^{-1}(\mathrm{e}^{\underline{\mathbf{A}}\,\Delta t_k} - \mathbf{I})\,\underline{\mathbf{B}},$$

$$\hat{\underline{\mathbf{B}}}_{k,1} = (\underline{\mathbf{A}}^{-1})^2(\mathrm{e}^{\underline{\mathbf{A}}\,\Delta t_k} - \underline{\mathbf{A}}\,\Delta \mathrm{t}_k - \mathbf{I})\,\underline{\mathbf{B}} \quad \text{and}$$

$$\hat{\underline{\mathbf{B}}}_{k,2} = \frac{2}{\Delta t_k}(\underline{\mathbf{A}}^{-1})^3\left(\mathrm{e}^{\underline{\mathbf{A}}\,\Delta t_k} - \frac{\underline{\mathbf{A}}^2\Delta \mathrm{t}_k^2}{2} - \underline{\mathbf{A}}\,\Delta \mathrm{t}_k - \mathbf{I}\right)\underline{\mathbf{B}}.$$

Assuming that the load is piecewise linear, $\mathrm{d}^2\mathbf{F}_k/\mathrm{d}t^2 = 0$, Eq. (13) yields the FOH solution discussed in Andersson [11]. The computational cost to include the second-order term can be expensive. However, fewer iterations are needed for the integration with the SOH method compared with the FOH method, and the accuracy of the solution can be improved.

The nodal rail displacements and velocities are then calculated using the superposition of the modal solutions, see Eq. (2)

$$\begin{Bmatrix} \mathbf{u} \\ \dot{\mathbf{u}} \end{Bmatrix} = \begin{bmatrix} \boldsymbol{\rho}^{(1)} & \cdots & \boldsymbol{\rho}^{(2M)} \\ \mathrm{i}\omega_1\boldsymbol{\rho}^{(1)} & \cdots & \mathrm{i}\omega_{2M}\boldsymbol{\rho}^{(2M)} \end{bmatrix} \begin{bmatrix} \underline{\mathbf{q}}_1 \\ \vdots \\ \underline{\mathbf{q}}_{2M} \end{bmatrix}. \tag{14}$$

3. Vehicle model

The vehicle model used in this study is discussed in Refs. [11,12]. The model is a representation of a driving (powered) bogie for a passenger train with two rigid wheelsets, a rigid bogie frame and linear primary suspensions (springs and dampings). Three-dimensional motion is accounted for. The equations of motion of the vehicle model are formulated in a floating frame of reference.

Two types of coordinate systems are used in the formulation: global and local coordinate systems. The global coordinate systems is the inertial frame of reference that is fixed in space and time. The local coordinate systems, one for each body of the vehicle system model, are body reference systems that move with respect to the global reference. The configuration of body i in the system is defined by two sets of coordinates, $\mathbf{u}^i_{v,f}$ and $\bar{\mathbf{u}}^i_{v,f}$ (overbar and subscript v denote body-fixed coordinates and vehicle model, respectively). The reference coordinates $\mathbf{u}^i_{v,f}$ define the global location of the reference frame of body i. The elastic coordinates $\bar{\mathbf{u}}^i_{v,f}$ describe the deformation of body i relative to that reference.

The elastic deformations are calculated using generalized flexible body coordinates $\mathbf{q}^i_{v,f}$ as

$$\bar{\mathbf{u}}^i_{v,f} = \mathbf{S}^i \mathbf{q}^i_{v,f}, \tag{15}$$

where $\mathbf{S}^i$ is a transformation matrix that normally involves some type of coordinate reduction. Thus, the generalized displacement vector $\mathbf{u}^i_v$ of body i contains both rigid body reference coordinates and flexible body coordinates

$$\mathbf{u}^i_v = \begin{bmatrix} \mathbf{u}^i_{v,f} \\ \mathbf{q}^i_{v,f} \end{bmatrix}. \tag{16}$$

With this choice of generalized coordinates, the equations of motion for body i can be written as

$$\mathbf{M}^i_v \ddot{\mathbf{u}}^i_v + \mathbf{C}^i_v \dot{\mathbf{u}}^i_v + \mathbf{K}^i_v \mathbf{u}^i_v = \mathbf{Q}^i_{v,e} + \mathbf{Q}^i_{v,v}, \tag{17}$$

where $\mathbf{M}^i_v$, $\mathbf{C}^i_v$ and $\mathbf{K}^i_v$ denote the mass, damping and stiffness matrix of the vehicle, respectively. Externally applied loads, such as gravity loads, wheel–rail contact loads and other interfacial loads between bodies in the vehicle, are assembled in $\mathbf{Q}^i_{v,e}$. Gyroscopic and circulatory effects are included in $\mathbf{Q}^i_{v,v}$.

After some reformulation, the equations of motion are rewritten and solved using a first-order formulation

$$\begin{bmatrix} \dot{\mathbf{u}}^i_v \\ \ddot{\mathbf{u}}^i_v \end{bmatrix} = -\begin{bmatrix} \mathbf{0} & -\mathbf{I} \\ (\mathbf{M}^i_v)^{-1}\mathbf{K}^i_v & (\mathbf{M}^i_v)^{-1}\mathbf{C}^i_v \end{bmatrix} \begin{bmatrix} \mathbf{u}^i_v \\ \dot{\mathbf{u}}^i_v \end{bmatrix} + \begin{bmatrix} \mathbf{0} \\ (\mathbf{M}^i_v)^{-1} \end{bmatrix} (\mathbf{Q}^i_{v,e} + \mathbf{Q}^i_{v,v}). \tag{18}$$

The vehicle model is coupled to the track model by wheel–rail contact force elements.

4. Wheel–rail contact geometry

As in most commercial multibody system (MBS) computer codes for simulation of vehicle dynamics, the wheel–rail contact geometry problem is here solved in advance. Contact geometry functions are calculated at several positions along the turnout due to the continuous variation in rail cross-section. Based on the current lateral displacement of the wheel centre with respect to the rail centre, the pre-calculated contact geometry functions are used in the form of look-up tables in the time integration analysis. The interpolation technique of the contact geometry functions discussed in Kassa et al. [12] is followed.

In each time step, the relative lateral wheel displacement that is used as input in the look-up tables is determined by summing the shortest distance between the wheel centre and the rail centre (which lies along the axis normal to the track centre line) and the local rail lateral displacement. The contact point locations are then interpolated from the look-up tables.

5. Coordinate transformations

From the time integration solution, the physical displacements and velocities of the vehicle and turnout are determined in the global coordinate system (cs). These values need to be transformed into local coordinate systems in order to determine local displacements and to calculate all contact forces and contact locations. The wheel–rail contact forces that have been calculated in the contact cs are then transformed back to the global cs to be used in the equations of motion.

A plan view of the nominal geometry of the turnout in the diverging route and the different coordinate systems are shown in Fig. 5. The coordinate systems used in the formulations are:

- global coordinate system (cs) $\{X_g, Y_g, Z_g\}$, fixed in time and space, with origin at the front of the turnout;
- track reference cs $\{x_t, y_t, z_t\}$ with origin on the track centre line moving with each wheelset;
- rail fixed cs $\{x_r, y_r, z_r\}$, parallel to the track reference cs, with origin at the rail centre (p_r in Figs. 5 and 6) to define the rail surface profile;
- wheel fixed cs $\{x_w, y_w, z_w\}$ with origin at the wheel centre to define the wheel surface profile;
- local beam element cs $\{\bar{x}_j, \bar{y}_j, \bar{z}_j\}$ of element j, with origin on the beam element j centre line, to describe nodal displacements and forces;
- contact cs $\{\xi_c, \eta_c, \zeta_c\}$ located at each contact point p_c, see Fig. 6.

5.1. Nodal displacement mapping

The nodal displacements and rotations of the rail beam elements in Eq. (14), $\mathbf{u}_i$ ($i = 1, 2, \ldots, 6$), are derived in the global cs. The corresponding values $\bar{\mathbf{u}}_i$ ($i = 1, 2, \ldots, 6$) in a local cs of a given beam element are derived using the rotational transformation matrix $\mathbf{T}$

$$\bar{\mathbf{u}}_i = \begin{bmatrix} \mathbf{T}_j & \mathbf{0} \\ \mathbf{0} & \mathbf{T}_j \end{bmatrix} \mathbf{u}_i, \tag{19}$$

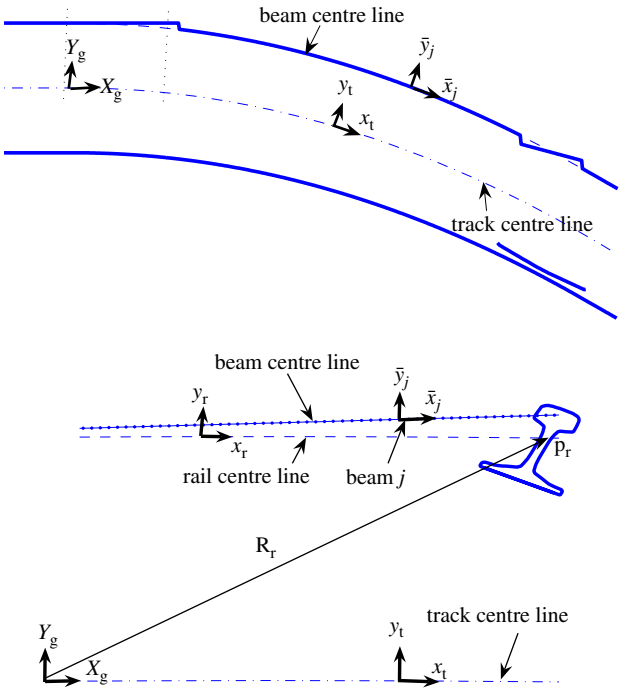

Fig. 5. Turnout geometry showing track, rail and beam element centre lines in the diverging route. Global and local coordinate systems are indicated.

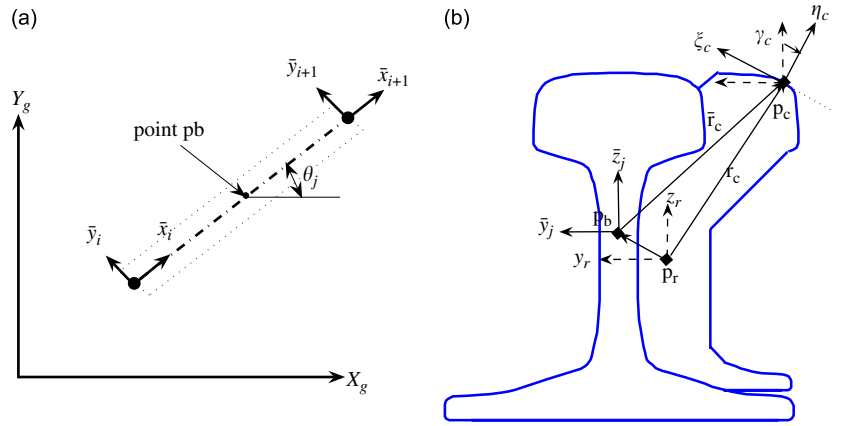

Fig. 6. Global cs and local cs at beam element nodes of beam element j (a), definition of contact coordinates with respect to rail and beam centre lines (b). Point p_b is located on the axis with the finite element rail nodes. Point p_r is always located on the rail centre line which is 0.75 m from the track centre line. Point p_c is the wheel–rail contact point.

where the transformation matrix $\mathbf{T}_j$ between the global cs $\{X_g, Y_g, Z_g\}$ and the local cs $\{\bar{x}_j, \bar{y}_j, \bar{z}_j\}$ of beam element j is expressed as

$$\mathbf{T}_j = \begin{bmatrix} \cos\theta_j & -\sin\theta_j & 0 \\ \sin\theta_j & \cos\theta_j & 0 \\ 0 & 0 & 1 \end{bmatrix}.$$

Here θ_j is the angle of beam element j with respect to the global cs, see Fig. 6. Similarly, the nodal velocities $\dot{\mathbf{u}}_i$ in the global cs are transformed into $\dot{\bar{\mathbf{u}}}_i$ in the local beam cs by using

$$\dot{\bar{\mathbf{u}}}_i = \begin{bmatrix} \mathbf{T}_j & \mathbf{0} \\ \mathbf{0} & \mathbf{T}_j \end{bmatrix} \dot{\mathbf{u}}_i. \tag{20}$$

Each wheel–rail contact point changes its location on the rail surface in every time step. Further, the FE nodes are located along beam axes which are not always on the centroidal axes of the rails. This means that displacements and forces at the contact points p_c on the rail surface need to be related with adjacent rail nodes by use of a transformation mapping. Mapping the nodal displacements of beam j at nodes i and $i+1$ to a point p_b on the beam centre line under the contact point is performed by using the beam shape function matrix $\mathbf{N}_b$. The displacement vector in point p_b is determined as

$$\bar{\mathbf{u}}_b = \mathbf{N}_b^{\mathrm{T}} \begin{bmatrix} \bar{\mathbf{u}}_i \\ \bar{\mathbf{u}}_{i+1} \end{bmatrix} = \underbrace{\mathbf{N}_b^{\mathrm{T}} \begin{bmatrix} \mathbf{T}_j & \mathbf{0} & \mathbf{0} & \mathbf{0} \\ \mathbf{0} & \mathbf{T}_j & \mathbf{0} & \mathbf{0} \\ \mathbf{0} & \mathbf{0} & \mathbf{T}_j & \mathbf{0} \\ \mathbf{0} & \mathbf{0} & \mathbf{0} & \mathbf{T}_j \end{bmatrix}}_{\mathbf{N}_{\mathrm{tot}}} \begin{bmatrix} \mathbf{u}_i \\ \mathbf{u}_{i+1} \end{bmatrix} = \mathbf{N}_{\mathrm{tot}} \begin{bmatrix} \mathbf{u}_i \\ \mathbf{u}_{i+1} \end{bmatrix}, \tag{21}$$

where $\mathbf{N}_{\mathrm{tot}}$ is the total mapping matrix for one contact point.

The displacements at contact point p_c on the rail surface are obtained from the displacements in point p_b on the beam centre line using

$$\mathbf{u}_c(1:3) = \bar{\mathbf{u}}_b(1:3) + \bar{\mathbf{u}}_b(4:6) \times \bar{\mathbf{r}}_c,$$

$$\mathbf{u}_c(4:6) = \bar{\mathbf{u}}_b(4:6), \tag{22}$$

where $\bar{\mathbf{r}}_c$ is the definition of the contact point position on the rail surface with respect to the beam centre line, see Fig. 6. Then, the global position $\mathbf{pos}_{\mathrm{rc}}$ of contact point p_c on the rail surface is obtained from the position

vector of point p_r and a contribution from the flexibility of the rail beam elements as

$$\mathbf{pos}_{\mathrm{rc}} = \mathbf{R}_r + \mathbf{A}_{g-t}^{\mathrm{T}}\mathbf{r}_c + \mathbf{T}_j^{\mathrm{T}}\mathbf{u}_c(1:3), \tag{23}$$

where $\mathbf{R}_r$ is the definition of the rail centre line (origin of rail fixed cs) in the global cs, see Fig. 5, and $\mathbf{r}_c$ is the position of the rail contact point in the rail fixed cs that defines the rail surface profile, see Fig. 6. $\mathbf{A}_{g-t}$ is a rotational transformation matrix from the global cs to the track reference cs.

Likewise, for a rigid wheel and wheel axle, the global position $\mathbf{pos}_{\mathrm{wc}}$ of the contact point on the wheel surface is defined by the global position of the wheel centre and the geometry of the wheel as

$$\mathbf{pos}_{\mathrm{wc}} = \mathbf{R}_w + \mathbf{A}_{g-t}^{\mathrm{T}}\mathbf{r}_w. \tag{24}$$

Here, $\mathbf{r}_w$ is the position vector of the wheel contact point with respect to the wheel centre in the track reference cs and $\mathbf{R}_w$ is the global position of the wheel centre (origin of wheel fixed cs). The contact point on the wheel surface with respect to the wheel centre in the wheel fixed cs is given by $\mathbf{L}_w$ (corresponding to $\mathbf{r}_c$ for the rail). The yaw angle φ of the rigid wheelset is used to transform the position vector $\mathbf{L}_w$ of the wheel contact point to the track reference cs as

$$\mathbf{r}_w = \mathbf{A}_{w-t}\mathbf{L}_w, \quad \mathbf{A}_{w-t} = \begin{bmatrix} \cos\varphi & -\sin\varphi & 0 \\ \sin\varphi & \cos\varphi & 0 \\ 0 & 0 & 1 \end{bmatrix}. \tag{25}$$

6. Wheel–rail contact forces

In analysis of dynamic train–track interaction, Hertz solution method for the normal wheel–rail contact problem is commonly used. Using the nonlinear Hertz theory, the relationship between the normal force and the normal deformation is given by

$$F_n = \begin{cases} C_H\delta_n^{(3/2)}, & \delta_n \geqslant 0, \\ 0, & \delta_n < 0. \end{cases} \tag{26}$$

To determine the normal deformation δ_n (see Fig. 7), the difference in the global positions of the contact points on the wheel and rail surfaces is calculated as

$$\mathbf{\Delta}_g = \mathbf{pos}_{\mathrm{rc}} - \mathbf{pos}_{\mathrm{wc}}. \tag{27}$$

Then, the local deformation $\mathbf{\Delta}_c$ of the wheel and rail surfaces in the local contact cs is obtained by transforming the deformation vector $\mathbf{\Delta}_g$ from the global to the local contact cs as

$$\mathbf{\Delta}_c = \mathbf{A}_c\mathbf{A}_{g-t}\mathbf{\Delta}_g, \tag{28}$$

where $\mathbf{A}_c$ is the transformation matrix from the track reference cs $\{x_t, y_t, z_t\}$ to the contact cs $\{\xi_c, \eta_c, \zeta_c\}$

$$\mathbf{A}_c = \begin{bmatrix} 0 & \cos\gamma_c & \sin\gamma_c \\ 0 & -\sin\gamma_c & \cos\gamma_c \\ 1 & 0 & 0 \end{bmatrix}.$$

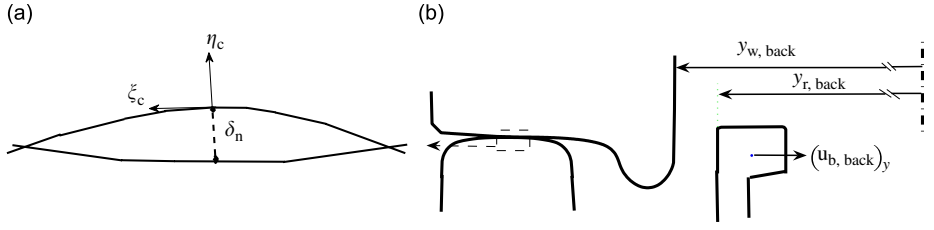

Fig. 7. Normal deformation at wheel–rail contact point on the rail head (a). Contact between check rail and back of wheel flange (b).

Here γ_c is the contact angle, see Fig. 6. At each time step, the normal component of the local deformation $\delta_n = (\mathbf{\Delta}_c)_\eta$ is determined and the normal contact force F_n is calculated using Eq. (26). To determine the tangential wheel–rail contact forces (creep forces and spin creep moment), the longitudinal, lateral and spin creepages are required. As the longitudinal velocity of the wheel is high compared with the lateral velocity, it is assumed that the predominant direction of velocity in the contact is parallel to the tangent of the track. The creepages in the contact plane, and the spin in the normal direction to the contact plane, are calculated from the relative velocities of wheel and rail at the contact point. As large spin creepages and multipoint contacts are common situations in turnout simulation, the creep forces are computed using the FASTSIM algorithm, which is based on the simplified theory of rolling contact, according to Kalker [15].

If there is contact between the check rail and the back of the wheel flange, this induces a constraint on the motion of the wheel. The check rail contact is modelled by a linear spring stiffness k_{back} in the direction normal to the contact plane. The spring stiffness is only activated if there is contact. The normal contact force acting on the back of the wheel flange is thus calculated as

$$F_{n,\text{back}} = \begin{cases} k_{\text{back}}\delta_{n,\text{back}} & \delta_{n,\text{back}} \geqslant 0, \\ 0 & \delta_{n,\text{back}} < 0. \end{cases} \tag{29}$$

The deformation $\delta_{n,\text{back}}$ normal to the contact surface is obtained from the difference in the positions of the contact points on the back of the wheel flange and on the side of the check rail. Knowing the position $y_{w,\text{back}}$ of the contact point on the back of the wheel flange in the track reference cs and the position of the side of the check rail $y_{r,\text{back}}$ with respect to the track centre, see Fig. 7, the normal deformation $\delta_{n,\text{back}}$ at the check rail contact is given by

$$\delta_{n,\text{back}} = y_{w,\text{back}} - (y_{r,\text{back}} + (\mathbf{A}_{b-t}\mathbf{u}_{c,\text{back}})_y), \tag{30}$$

where $\mathbf{u}_{c,\text{back}}$ is the displacement vector of the check rail beam element at the contact point, *cf* $\mathbf{u}_c$ in Eq. (22). The transformation matrix $\mathbf{A}_{b-t}$ is used to transform a displacement of a point on the check rail beam centre line from the local cs $\{\bar{x}_j, \bar{y}_j, \bar{z}_j\}$ of beam element j to the track reference cs $\{x_t, y_t, z_t\}$.

For the tangential direction, full sliding between the wheel and the check rail is assumed. The friction coefficient in the check rail contact is denoted μ_{back}. The directions of the tangential contact forces are determined by the yaw angle of the wheelset and the difference in the rolling and sliding velocities of the back of the wheel flange contact point. The forces at the contact between the back of the wheel flange and the check rail in the track reference cs are given as

$$\mathbf{F}_{\text{back},t} = F_{n,\text{back}} \begin{bmatrix} S_x\mu_{\text{back}} \\ 1 \\ S_z\mu_{\text{back}} \end{bmatrix}. \tag{31}$$

Here S_x and S_z define the directions of the tangential contact forces. Direction S_x is determined by the sign of the difference in the rolling and sliding velocities of the wheel flange contact point as

$$S_x = \begin{cases} +1 & \text{if } (v - \omega_v r_{w,\text{back}}) > 0, \\ 0 & \text{if } (v - \omega_v r_{w,\text{back}}) = 0, \\ -1 & \text{if } (v - \omega_v r_{w,\text{back}}) < 0. \end{cases}$$

The sign S_z is determined by the sign of the yaw angle of the wheelset

$$S_z = \begin{cases} -1 & \text{if } \varphi > 0, \\ 0 & \text{if } \varphi = 0, \\ +1 & \text{if } \varphi < 0. \end{cases}$$

6.1. Contact forces mapping

The vehicle motion acting on the vehicle model is influenced by the external forces. The wheel–rail contact forces described above contribute to the external load vector in the vehicle model. Here, as the wheels are assumed rigid, the contact forces are easily mapped to forces acting on the wheel centre. This is done by first mapping the contact forces $\mathbf{F}_c$ and the spin moments $\mathbf{M}_c$ from the contact coordinate systems to the track reference cs as

$$\begin{bmatrix} \mathbf{F}_{\mathrm{wr},t} \\ \mathbf{M}_{\mathrm{wr},t} \end{bmatrix} = \begin{bmatrix} \mathbf{A}_c^{\mathrm{T}} & \mathbf{0} \\ \mathbf{0} & \mathbf{A}_c^{\mathrm{T}} \end{bmatrix} \begin{bmatrix} \mathbf{F}_c \\ \mathbf{M}_c \end{bmatrix}. \tag{32}$$

Then, the equivalent loading on the centre of the wheel in the global cs is obtained as

$$\mathbf{F}_w = \begin{bmatrix} \mathbf{A}_{g-t}^{\mathrm{T}} \mathbf{F}_{\mathrm{wr},t} \\ \mathbf{A}_{g-t}^{\mathrm{T}} (\mathbf{r}_w \times \mathbf{F}_{\mathrm{wr},t} + \mathbf{M}_{\mathrm{wr},t}) \end{bmatrix}. \tag{33}$$

The contribution of the contact force at the back of the wheel flange to the equivalent wheel loading is given by

$$\mathbf{F}_{w,\mathrm{back}} = -\begin{bmatrix} \mathbf{A}_{g-t}^{\mathrm{T}} \\ \mathbf{A}_{g-t}^{\mathrm{T}} \tilde{\mathbf{r}}_{w,\mathrm{back}} \end{bmatrix} \mathbf{F}_{\mathrm{back},t}, \tag{34}$$

where $\tilde{\mathbf{r}}_{w,\mathrm{back}}$ is the skew-symmetric matrix associated with the vector $\mathbf{r}_{w,\mathrm{back}}$. The total equivalent load vector, which contributes to the external load vector in the vehicle model, is the sum of the equivalent contact loads in all wheel–rail contact points.

$$\mathbf{F}_{w,\mathrm{tot}} = \sum \mathbf{F}_w + \mathbf{F}_{w,\mathrm{back}}. \tag{35}$$

The contact forces $\mathbf{F}_c$ and the spin moments $\mathbf{M}_c$ induced by the moving loads are mapped onto the rails as nodal forces and moments. The contact loads $(\mathbf{F}_{\mathrm{wr},t}, \mathbf{M}_{\mathrm{wr},t})$ in the track reference cs, defined in Eq. (32), are mapped onto the rail beam centre line point p_b as

$$\begin{bmatrix} \mathbf{F}_r \\ \mathbf{M}_r \end{bmatrix}_{p_b} = \begin{bmatrix} -\mathbf{A}_{b-t}^{\mathrm{T}} \mathbf{F}_{\mathrm{wr},t} \\ -\mathbf{A}_{b-t}^{\mathrm{T}} \mathbf{M}_{\mathrm{wr},t} - \tilde{\bar{\mathbf{r}}}_c \mathbf{A}_{b-t}^{\mathrm{T}} \mathbf{F}_{\mathrm{wr},t} \end{bmatrix} = -\begin{bmatrix} \mathbf{I} \\ \tilde{\bar{\mathbf{r}}}_c \end{bmatrix} \mathbf{A}_{b-t}^{\mathrm{T}} \mathbf{F}_{\mathrm{wr},t} - \begin{bmatrix} \mathbf{0} \\ \mathbf{I} \end{bmatrix} \mathbf{A}_{b-t}^{\mathrm{T}} \mathbf{M}_{\mathrm{wr},t}. \tag{36}$$

Here $\tilde{\bar{\mathbf{r}}}_c$ is the skew-symmetric matrix associated with the vector $\bar{\mathbf{r}}_c$. Then, the forces at point p_b are mapped onto nodal loads using the total load mapping matrix $\mathbf{N}_{\mathrm{tot}}$, see Eq. (21), as

$$\begin{bmatrix} \mathbf{F}_i \\ \mathbf{M}_i \\ \mathbf{F}_{i+1} \\ \mathbf{M}_{i+1} \end{bmatrix} = \mathbf{N}_{\mathrm{tot}}^{\mathrm{T}} \begin{bmatrix} \mathbf{F}_r \\ \mathbf{M}_r \end{bmatrix}_{p_b}. \tag{37}$$

These nodal loads contribute to the generalized load vector $\mathbf{F}$ in Eq. (5).

7. Numerical examples and discussion

To demonstrate the influence of the detailed track model, examples from simulations of the dynamic interaction between the bogie model and the turnout model are presented in this section. A vehicle with axle load 20 tonnes and train speed 60 km/h is used. The geometry of the turnout is the standard design UIC60-760-1:15 with curve radius 760 m and crossing angle 1:15. The simulations were performed for the vehicle model running along the diverging route of the turnout in facing move (from the switch panel to the crossing panel). Coefficients of friction at the wheel–rail contacts and for contact at the back of the wheel flange are taken as $\mu = 0.3$ and $\mu_{\mathrm{back}} = 0.15$, respectively. A linearized Hertzian contact stiffness $k_H = 1\,\mathrm{GN/m}$ for

wheel–rail normal contact and a contact stiffness $k_{\text{back}} = 1\,\text{GN/m}$ for contact at the back of the wheel flange are used.

The total length of the FE model of the turnout is 60 m. Each railpad is represented by four linear springs in each direction with total stiffness 240 MN/m in the vertical direction and 120 MN/m in the horizontal directions. Linear springs under the sleeper nodes are used to represent the ballast/subgrade stiffness. The stiffness values are 50 MN/m in the vertical direction and 25 MN/m in the horizontal directions.

Real-valued modal parameters were calculated in the FEM software. Several modes in the lower eigenfrequency regime are related to the longitudinal displacement of sleepers. Since the influence of such modes on the vertical and lateral wheel–rail contact forces is not significant, the track dofs in the longitudinal direction were constrained to zero. Several elastic modes of the sleepers are also present in the lower eigenfrequency regime. However, in Ref. [16], good agreement between measured and simulated vertical contact forces was observed when using a track model with rigid sleepers. On that note, the sleeper beam element properties were set to rigid. The rail boundaries of the model are clamped. The output file from the FEM software included nodal coordinates for the rail beam elements in the diverging route, mode shapes, eigenfrequencies and modal masses. The number of rail dofs in the diverging route is 9408. The data file together with the assumed modal damping values, described in Section 2.1, were used to form the equations of motion of the turnout model. Wheel–rail contact geometry functions were pre-calculated at 36 positions along the turnout using the software GENSYS [17]. Linear interpolation between two adjacent locations with pre-calculated contact functions was used to determine the contact conditions at intermediate positions.

7.1. Convergence study

In the first example, a convergence study is performed with an increasing number of eigenmodes of the flexible turnout model. The eigenfrequencies of the first 500 modes of the turnout model are shown in Fig. 8. The eigenfrequencies are neither well separated nor clustered in specific frequency regions. Using the procedure presented in Section 2.1, complex-valued modal parameters for the lowest 500 eigenmodes were determined. Some examples of modes of vibration are shown in Figs. 9 and 10. The modes corresponding to the lowest eigenfrequencies are dominated by lateral deformation as shown in Fig. 9. Fig. 10 shows the first five vertical vibration modes of the rails and sleepers on the ballast.

Simulations of the dynamic interaction between bogie and turnout were performed using 10, 50, 100, 250 or 500 eigenmodes. Fig. 11 shows the lateral creep force and the normal contact force in the switch panel when using 250 modes for the FOH and SOH methods. Two-point contact situation, one on the stock rail and the other on the switch rail, is observed at a transition region in between 3.5 and 7.5 m, then after, the wheel is

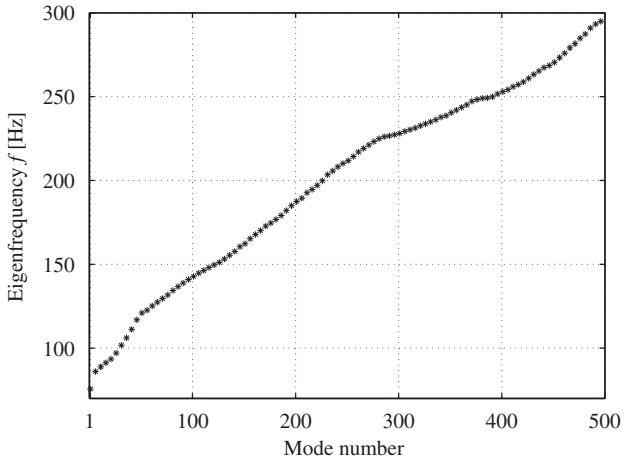

Fig. 8. Eigenfrequencies of the first 500 modes.

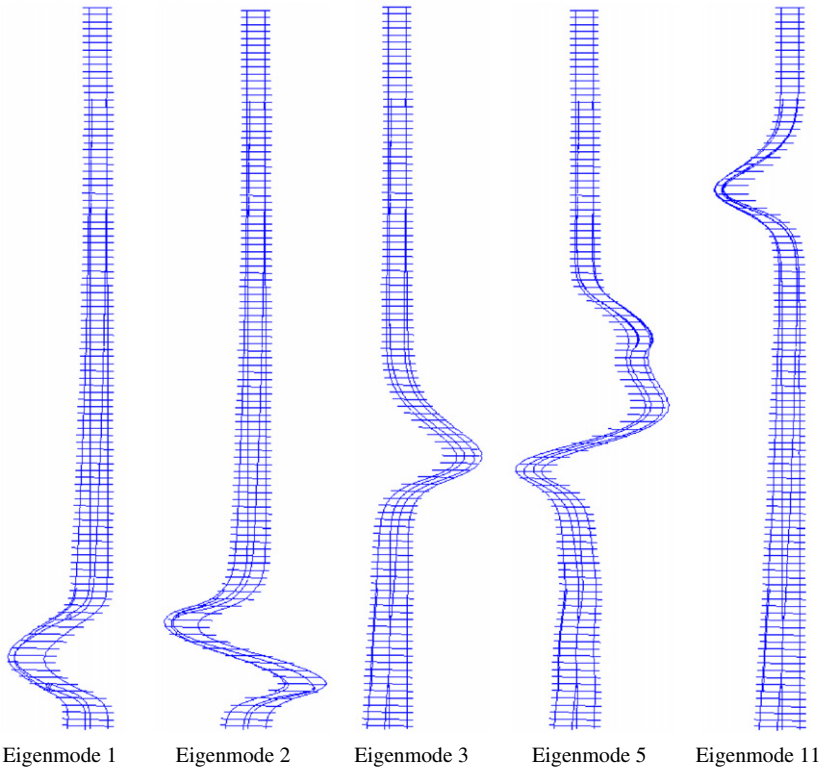

Fig. 9. Eigenmodes 1, 2, 3, 5 and 11 of the turnout model with undamped eigenfrequencies $f_1 = 75.6$ Hz, $f_2 = 80.6$ Hz, $f_3 = 84.3$ Hz, $f_5 = 85.7$ Hz and $f_{11} = 88.8$ Hz. Lateral deformation is dominating for these modes.

fully supported by the switch rail. Very similar results were obtained for the FOH and SOH methods as shown in Fig. 11. In Table 1, the maximum eigenfrequency included and the simulation time using FOH and SOH for the five chosen number of eigenmodes are listed. Using 250 eigenmodes, eigenfrequencies up to 211.5 Hz are included. The difference in simulation times using the two transient solution methods, FOH or SOH, was not significant, see Table 1. The simulations were performed on a PC with an Intel(R) Core processor.

Figs. 12–17 show simulation results using several eigenmodes. The lateral displacement of the leading wheelset is shown in Fig. 12 using 10, 50, 100, 250 or 500 eigenmodes. The positive displacement indicates that the wheelset is displaced outwards in the curve. The large lateral wheelset displacements at distances 0 and 51 m are due to the abrupt changes in track curvature at the front and rear of the turnout. In Fig. 13, the lateral displacement is displayed with more detail at three sections: the switch panel (A), the closure panel (B) and the crossing panel (C).

The influence of the number of modes on the lateral and vertical wheel–rail contact forces are presented in Figs. 14–17. The presented contact force in either the vertical or the lateral direction is the sum of the wheel–rail contact forces (in cases of multiple contact) for each wheel/rail combination. Due to the constant variation in rail profile, discontinuities in the contact condition and contact point jumps in the switch and crossing panels, the lateral and vertical contact forces reach peak values. The contact forces reach a steady-state condition in the closure panel, where the rail profiles are constant. The calculated lateral contact force using 100, 250 or 500 modes is shown in Fig. 14, and in more detail, for the switch panel (A) and the crossing panel (C) in Fig. 15. The resulting force has converged in the switch panel when using 250 modes. The vertical contact force for different numbers of eigenmodes is studied in Figs. 16 and 17. Again, the resulting force has converged in the switch panel when using 250 modes. However, a larger number of modes may be required to obtain accurate results in the crossing panel if higher resonance frequencies are excited by discontinuities or irregularities in the switch and crossing panels.

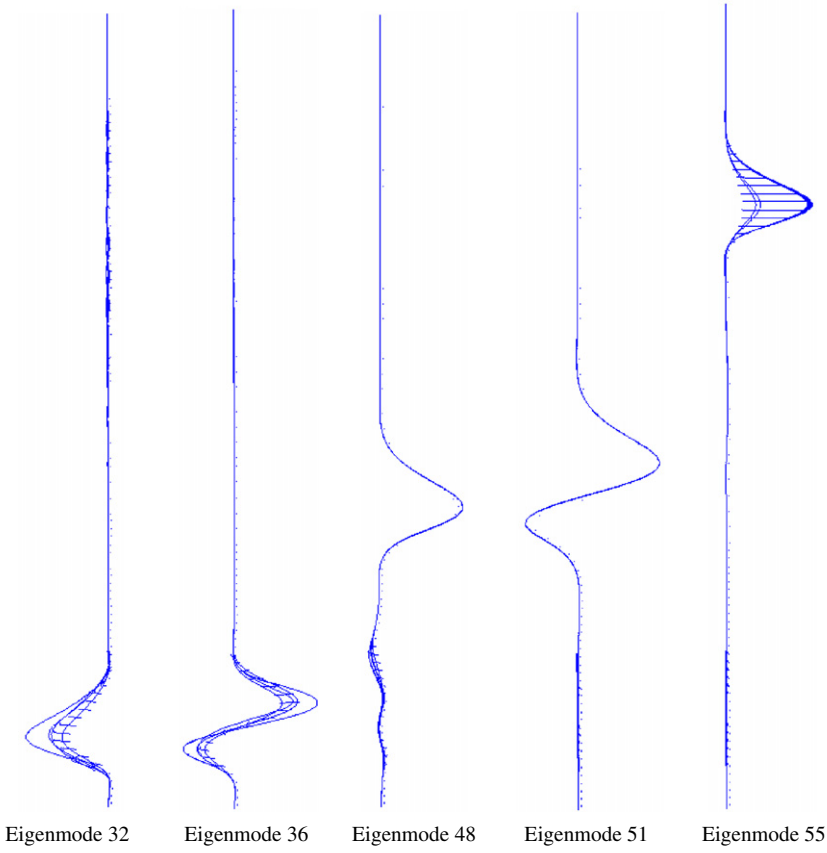

Fig. 10. Eigenmodes 32, 36, 48, 51 and 55 of the turnout model with undamped eigenfrequencies $f_{32} = 101.8\,\text{Hz}$, $f_{36} = 106.1\,\text{Hz}$, $f_{48} = 119.2\,\text{Hz}$, $f_{51} = 121.0\,\text{Hz}$ and $f_{55} = 122.3\,\text{Hz}$. Vertical deformation is dominating for these modes.

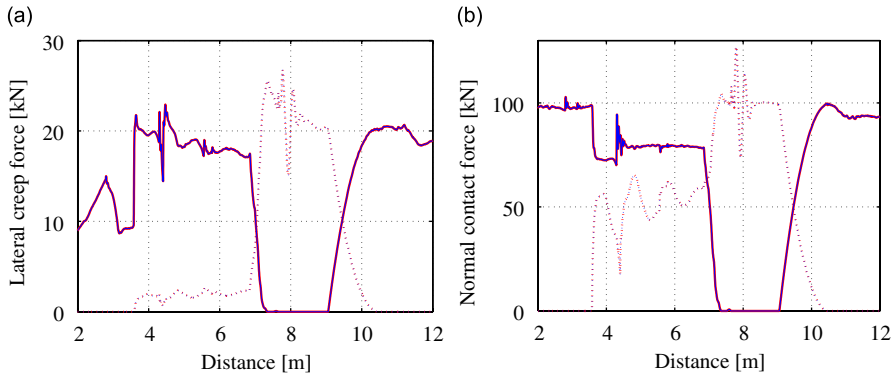

Fig. 11. Lateral creep force (a) and normal contact force (b) in the switch panel when using 250 modes. Solid lines correspond to the first contact point while broken lines correspond to the second contact point. Thick lines (solid or broken line) are based on SOH method solutions while thin lines (solid or broken line) correspond to FOH solutions. The thick and thin lines are overlapping.

7.2. Comparison between GENSYS and DIFF3D simulation results

In a previous study, a multibody model of dynamic interaction between a bogie and the UIC60-760-1:15 turnout was developed using the commercial software GENSYS [17]. It was compared with DIFF3D results when using a rigid track model [12]. In the second example, simulations with GENSYS and DIFF3D are

Table 1
Simulation times using different numbers of modes M for the turnout model

Number of modes M	Maximum eigenfrequency f (Hz)	Simulation time (h)	
		SOH	FOH
10	88.4	2.559	2.823
50	119.9	3.919	3.838
100	142.7	5.419	5.101
250	211.5	13.841	14.711
500	296.8	89.443	–

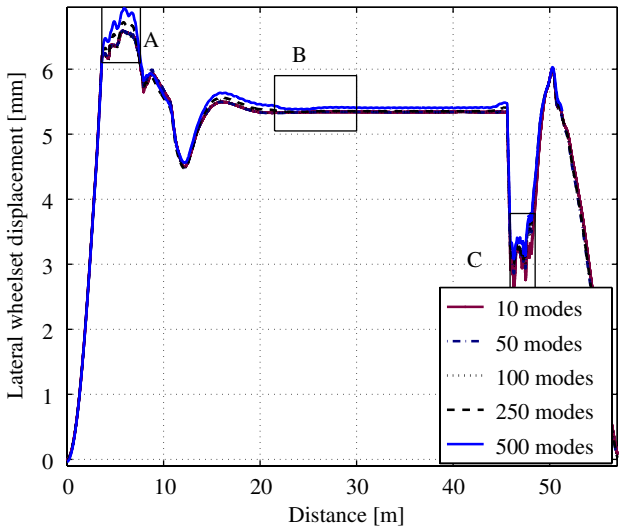

Fig. 12. Lateral displacement of the leading wheelset.

compared when using a flexible track model. Note that the track model used in GENSYS is a simple mass-spring-damper model with few dofs (seven dofs) that is coupled to each wheelset of the vehicle model [1].

Results from using the simple track model in GENSYS are compared with analyses using the complex FE model of the turnout in Figs. 18 and 19. For comparison, DIFF3D results based on modal models with either 10 modes or 500 modes are shown. In the closure panel, where the rail cross-sections and the track properties are relatively constant, good agreement between GENSYS and DIFF3D is obtained for both 10 and 500 modes. However, in the crossing panel, the maximum lateral contact force from GENSYS is about 50 % lower than the corresponding force when using 500 modes in DIFF3D, see Fig. 18.

Finally, the lateral wheelset displacement using DIFF3D with either 10 or 500 flexible modes is compared with GENSYS results in Fig. 19. Apart from some differences in the switch panel (at around 8–10 m) and in the crossing panel, the agreement between the two computer programs is good.

7.3. Discussion

In order to simulate turnout degradation, such as wear and plastic deformation of rail profiles, an accurate prediction of wheel–rail contact force magnitudes is necessary. Previous measurements of wheel–rail contact forces in a turnout have shown that the high-frequency contribution to the vertical contact force in the crossing panel is significant, see Fig. 2. Thus, in order to improve the accuracy of calculated contact forces compared to traditional methods [4–6], the approach used in this paper is to study dynamic train–turnout interaction in a wider frequency range by including a detailed turnout model. In this model, the flexibility of rails and sleepers in bending and torsion may be accounted for.

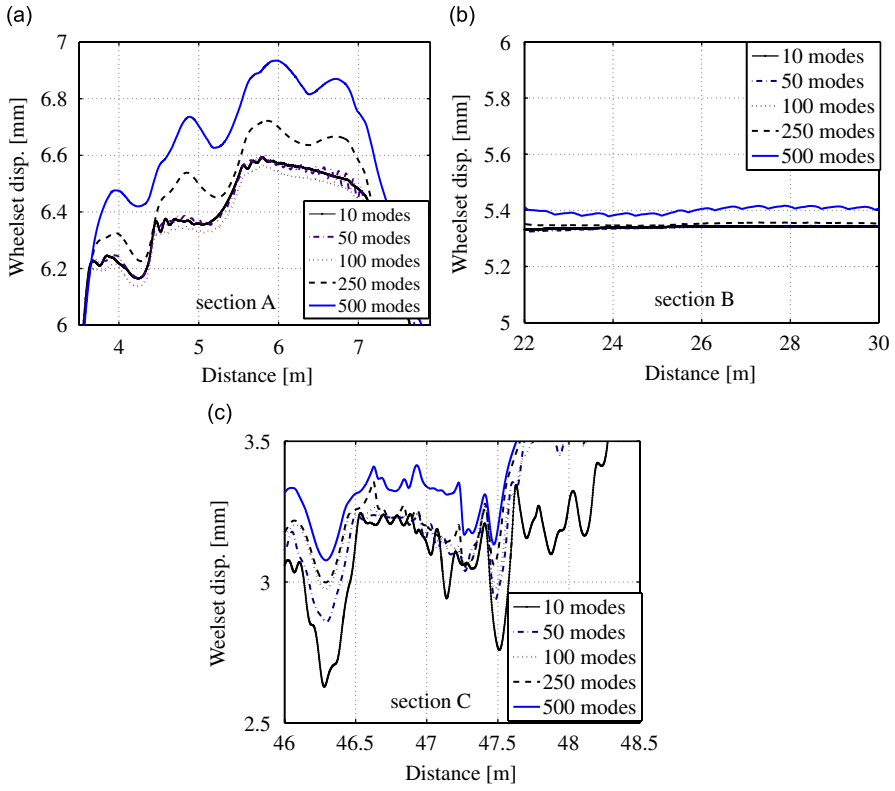

Fig. 13. Lateral wheelset displacement zoomed at section A (a), section B (b) and section C (c) in Fig. 12.

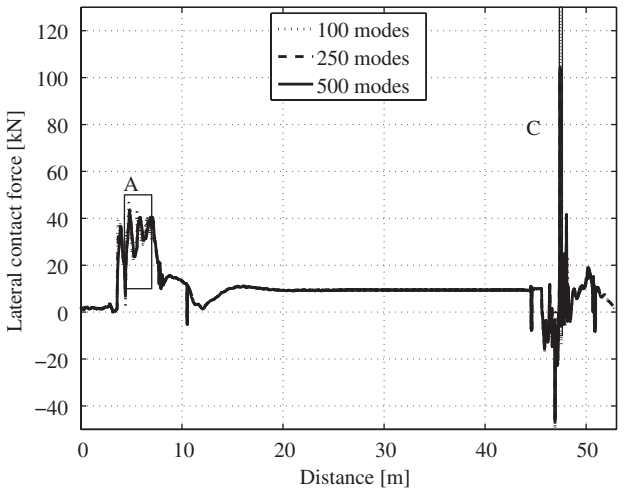

Fig. 14. Lateral wheel–rail contact force on the outer wheel of the leading wheelset.

It is observed from Figs. 12 and 13 that even with 500 modes, the wheelset displacement has not yet fully converged. However, the main features of the response are captured already with 10 modes as this response is mainly dependent on the low-frequency vehicle dynamics and the nominal turnout geometry, see Fig. 19. Therefore, it is suggested that for investigations of vehicle dynamics, acceptable results can be obtained with only a few flexible modes of the track model.

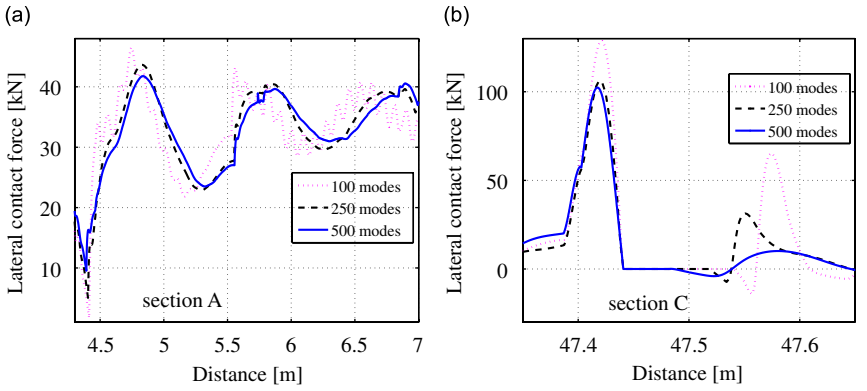

Fig. 15. Lateral wheel–rail contact force on the outer wheel of the leading wheelset zoomed at section A (a) and section C (b) in Fig. 14.

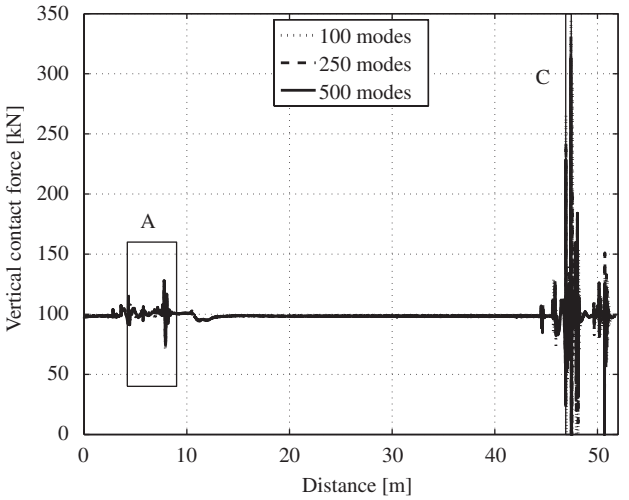

Fig. 16. Vertical wheel–rail contact force on the outer wheel of the leading wheelset.

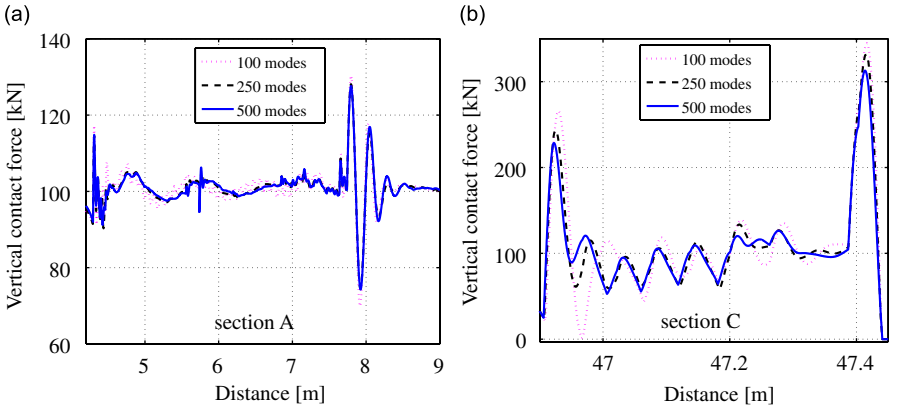

Fig. 17. Vertical wheel–rail contact force on the outer wheel of the leading wheelset zoomed at section A (a) and section C (b) in Fig. 16.

It is shown that the lateral wheel–rail contact forces in the switch and closure panels has converged when modes up to 200 Hz are included. This means that the important features of lateral wheel–rail interaction, such as the lateral motion of rails and sleepers on the ballast at about 75–100 Hz and the lateral vibration of the

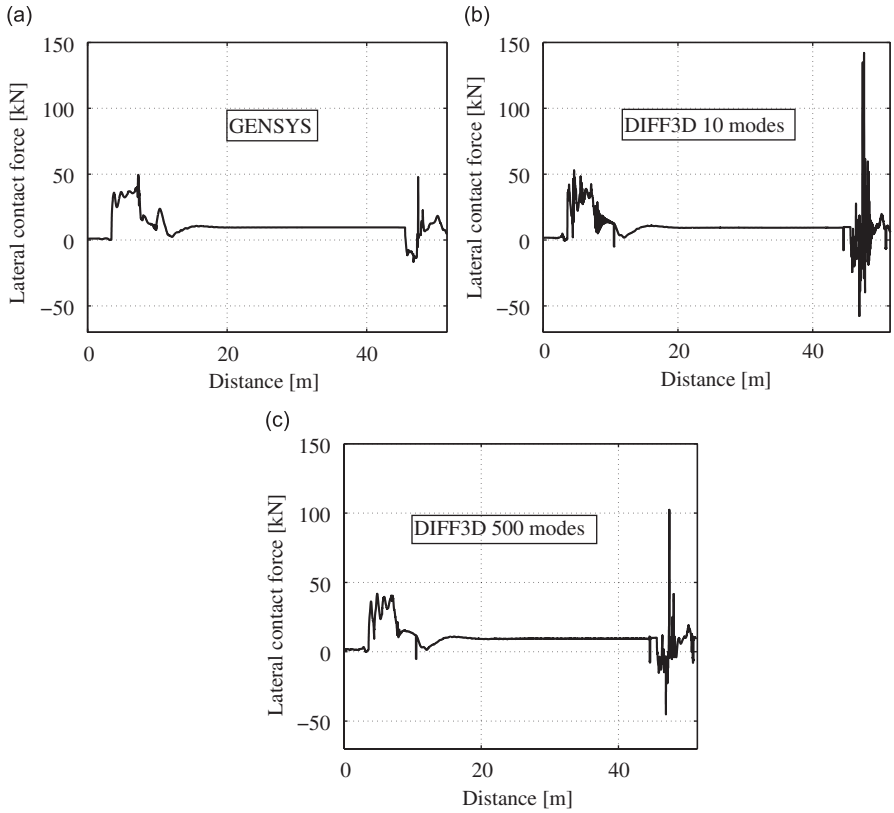

Fig. 18. Lateral wheel–rail contact forces on the outer wheel of the leading wheelset using GENSYS (a), DIFF3D with 10 modes (b) and DIFF3D with 500 modes (c).

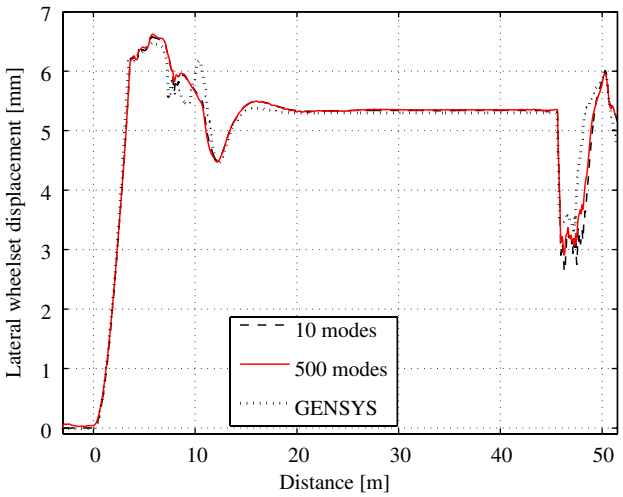

Fig. 19. Lateral wheelset displacement along the turnout using GENSYS, DIFF3D with 10 modes and DIFF3D with 500 modes.

rails on the railpad at about 150–200 Hz are accounted for. However, in the crossing panel, the calculated wheel–rail contact forces have not converged when using 500 modes. A larger number of modes that include vertical vibration of the rails on the railpads is required in the analysis. Since computational times are

excessive already with 500 modes, a more efficient modal reduction method that identifies and includes the most significant modes is needed.

8. Concluding remarks

A FE model of a standard turnout design has been built using a commercial computer program. The model includes the structural dynamic flexibility of rails, rail pads and sleepers on ballast, and it carefully takes into account the spatial distribution of mass and stiffness along the turnout. Based on calculated real-valued modal parameters from the commercial software and assumed relative modal dampings, complex-valued modal parameters were determined to describe the turnout as a modal component in the in-house software DIFF3D for simulation of dynamic train–track interaction.

The described method improves the accuracy of the results from the train–track interaction simulations as it takes into account dynamic excitation in an extended frequency range compared to most commercial computer programs for vehicle dynamics. In particular, the magnitudes of wheel–rail contact forces are sensitive to high-frequency impact excitation in the switch and crossing panels. In addition, the response (such as displacements and sectional forces) of the various rails and sleepers in the turnout can be investigated.

For the track subsystem, first-order hold (FOH) and second-order hold (SOH) time integration solution methods were compared. Simulations were performed using the first 500 modes. The highest eigenfrequency was about 300 Hz. The influence of the number of modes on the convergence of wheel–rail contact forces and wheelset displacement was studied. Even 500 modes was not fully sufficient for the wheelset displacement, whereas the lateral contact forces seemed to have converged when 250 modes were accounted for. Thus, to improve accuracy a larger number of modes may be required as some of the significant resonances, such as the torsional and pinned–pinned resonance frequencies of the rails, are well above 300 Hz.

The simulation time increases rapidly with increasing numbers of modes in the modal superposition. To reduce simulation time, a modal superposition method that identifies and excludes less important modes (depending on type and location of the calculated response) would be useful.

Acknowledgements

This work was performed as part of the activities within CHARMEC (CHAlmers Railway MEChanics), see (www.charmec.chalmers.se). Mrs. Maria Andrén of Epsilon HighTech AB built the FE model of the turnout. Input data on rail cross-sections in the turnout were supplied by Mr Erich Scheschy of VAE GmbH.

References

[1] E. Kassa, Simulation of Dynamic Interaction between Train and Turnout, Lic Thesis, Department of Applied Mechanics, Chalmers University of Technology, Gothenburg, Sweden, 2004, 56pp.
[2] K. Knothe, S.L. Grassie, Modelling of railway track and vehicle/track interaction at high frequencies, *Vehicle System Dynamics* 22 (1993) 209–262.
[3] S.L. Grassie, Dynamic models of the track and their uses, *FRA/ERRI Conference*, TU Delft, 24–26 June, 1992, Kluwer Academic Publisher, Dordrecht, 1992, pp. 165–183.
[4] S. Gurule, N. Wilson, Simulation of wheel/rail interaction in turnouts and special track work, *Supplement to Vehicle System Dynamics* 33 (1999) 143–154 (Lisse, The Netherlands: Swets & Zeitlinger).
[5] G. Schupp, H. Netter, L. Mauer, M. Gretzschel, Multibody system simulation of railway vehicles with SIMPACK, *Supplement to Vehicle System Dynamics* 31 (1999) 101–109 (Lisse, The Netherlands: Swets & Zeitlinger).
[6] J.R. Oswald, G. Bishop, Optimization of turnout layout and contact geometry through dynamic simulation of vehicle–track interaction, *Proceedings of the 7th International Heavy Haul Conference*, Brisbane, Australia, 2001, pp. 31–35.
[7] S. Iwnicki, Results of Manchester benchmarks, *Vehicle System Dynamics* 31 (1999) 2–12.
[8] E. Kassa, J.C.O. Nielsen, *Dynamic interaction between train and railway turnout—full-scale field test and validation of simulation models*, Department of Applied Mechanics, Chalmers University of Technology, Gothenburg, Sweden, 2007 16pp.
[9] C. Andersson, T. Dahlberg, Wheel/rail impacts at a railway turnout crossing, *Proceedings ImechE, Part F, Journal of Rail and Rapid Transit* 212 (F2) (1998) 123–134.
[10] SDRC I-DEAS Master Series, Student Guide, second ed., 1994.

[11] C. Andersson, Modelling and Simulation of Train–track Interaction including Wear Prediction, PhD Thesis, Department of Applied Mechanics, Chalmers University of Technology, Gothenburg, Sweden, 2003.
[12] E. Kassa, C. Andersson, J.C.O. Nielsen, Simulation of dynamic interaction between train and railway turnout, *Vehicle System Dynamics* 44 (2006) 247–258.
[13] T.J.S. Abrahamsson, Modal Analysis and Synthesis in Transient Vibration and Structural Optimization Problems, PhD Dissertation, Department of Solid Mechanics, Chalmers University of Technology, Gothenburg, Sweden, 1990.
[14] L. Meirovitch, *Principles and Techniques of Vibrations*, Prentice-Hall, Upper Saddle River, New Jersey, 1997, p. 694.
[15] J.J. Kalker, A fast algorithm for the simplified theory of rolling contact, *Vehicle System Dynamics* 11 (1982) 1–13.
[16] J.C.O. Nielsen, High-frequency vertical wheel–rail contact forces—validation of a prediction model by field testing, *Proceedings of the 7th International Conference on Contact Mechanics and Wear of Rail/Wheel Systems (CM2006)*, Brisbane, Australia, 2006, pp. 41–48.
[17] GENSYS User's Manual, 2004, Release 0403, Available on line at: http://www.gensys.se/.